A framework for detailed numerical simulation of patient-specific cerebrospinal fluid flow for relevant clinical applications

Edgaras Misiulis, Algis Dziugys, Alina Barkauskiene, Aidanas Preiksaitis, Vytenis Ratkunas, Gediminas Skarbalius, Robertas Navakas, Tomas Iesmantas, Robertas Alzbutas, Saulius Lukosevicius, Mindaugas Serpytis, Saulius Rocka, Indre Lapinskiene, Vytautas Petkus

Corresponding author: Edgaras Misiulis is with the Laboratory of Heat-Equipment Research and Testing, Lithuanian Energy Institute, Breslaujos st. 3, Kaunas 44403, Lithuania (e-mail: edgaras.misiulis@lei.lt, tel. nr. +37060377878).

Gediminas Skarbalius, Robertas Navakas and Algis Dziugys are with the Laboratory of Heat-Equipment Research and Testing, Lithuanian Energy Institute, Breslaujos st. 3, Kaunas 44403, Lithuania (e-mail: gediminas.skarbalius@lei.lt; robertas.navakas@lei.lt; algis.dziugys@lei.lt).

Indre Lapinskiene and Mindaugas Serpytis are with the Clinic of Anaesthesiology and Intensive Care, Faculty of Medicine, Vilnius University, M. K. Ciurlionio st. 21, Vilnius 03101, Lithuania (e-mail: indre.lapinskiene@santa.lt; mindaugas.serpytis@santa.lt).

Saulius Rocka and Aidanas Preiksaitis are with the Clinic of Neurology and Neurosurgery, Faculty of Medicine, Vilnius University, M. K. Ciurlionio st. 21, Vilnius 03101, Lithuania (e-mail: saulius.rocka@santa.lt; aidanas.preiksaitis@santa.lt).

Alina Barkauskiene is with the Center for Radiology and Nuclear Medicine, Vilnius University Hospital Santaros Klinikos, Santariskiu st. 2, Vilnius 08661, Lithuania (e-mail: alina.barkauskiene@santa.lt).

Vytenis Ratkunas and Saulius Lukosevicius are with the Department of Radiology, Lithuanian University of Health Sciences, Eiveniu st. 2, Kaunas 50009, Lithuania (e-mail: vytenis.ratkunas@lsmu.lt; saulius.lukosevicius@lsmu.lt).

Tomas Iesmantas and Robertas Alzbutas are with the Department of Mathematics and Natural Sciences, Kaunas University of Technology, K. Donelaicio st. 73, Kaunas 44249, Lithuania (e-mail: tomas.iesmantas@ktu.lt; robertas.alzbutas@ktu.lt).

Vytautas Petkus is with the Health Telematics Science Institute, Kaunas University of Technology, K. Donelaicio st. 73, Kaunas 44249, Lithuania (e-mail: vytautas.petkus@ktu.lt).

***Abstract*:**

Background and Objectives: **Recently, computational fluid dynamics simulations were used to model cerebrospinal fluid (CSF) flow in a simplified subarachnoid space (SAS), in which SAS geometry was coarsened and smoothed, thereby, losing the periarterial spaces and bays common to SAS, which could play a crucial role for the resulting patient's outcome after subarachnoid hemorrhage (SAH). Our objective was to develop a computational framework for CSF flow numerical finite element method (FEM) based model that incorporates detailed patient-specific cranial CSF space (cCSFS) combining ventricular system, SAS, and periarterial spaces reconstructed from the T_2-weighted magnetic resonance imaging (MRI). Following model is useful when considering the clearance of unwanted substances such as leaked blood resulting from the aneurysmal rupture or when considering the drug spreading in CSF spaces. In addition, the inclusion of periarterial spaces allows evaluation of the direct contact between cerebrospinal fluid, parenchyma and artery walls.**

Methods: **A single, healthy, 42 years white old male was enrolled in this study. The 3D Slicer software was used for the cCSFS volume segmentation, while the COMSOL Multiphysics® v6.0 was used for CSF flow pattern prediction. The projection operations were used to analyze the cranial CSF space geometrical and CSF flow parameters.**

Results: **We demonstrated that the computational effort can be significantly reduced without cCSFS coarsening. This was achieved by using first-order finite elements instead of second-order ones. Lower finite elements order resulted in only 1.4 % difference in simulated transmantle pressures, and lower than 10 % difference in momentum in about 90 % of all elements, while the time required to model the CSF flow was reduced about four times from ~20 min to ~5 min, and the random access memory usage was reduced about five times from ~150 GB to ~30 GB. Our model showed that a constant net CSF flow of 500 ml/day was maintained, while the transmantle pressure was 1.8 Pa.**

Conclusions: **The presented CSF flow model holds promise in becoming a viable tool for the timely prediction of CSF flow pathways after SAH.**

***Index Terms*: Computational fluid dynamics, cerebrospinal fluid, subarachnoid space, patient-specificity, periarterial space.**

I. Introduction

Computational fluid dynamics (CFD) and numerical methods have become one of the viable investigation methods allowing to test various cerebrospinal fluid (CSF) flow hypothesis, including investigations on CSF flow driving mechanisms in the perivascular spaces [1], [2], [3], [4], [5], [6], investigations on blood removal efficiency from CSF in post-subarachnoid hemorrhage patients [7], [8], [9], investigations on the CSF flow dynamics [10], drug delivery via CSF pathways [11] and to evaluate parameters that otherwise are impossible to evaluate *in vivo,* such as dynamics of transmantle pressure gradient under various conditions [12].

These modelling applications extend from modelling specific isolated anatomical structures, such as single ventricle, spinal canal, to encompassing whole subarachnoid space region, including cerebral ventricular system. In addition, some of these studies also incorporate time-dependent CSF flow disturbances due to breathing, cardio cycles etc.

Based on these studies, it can be concluded that numerical modelling of the whole subarachnoid space (SAS) requires extensive amount of computational power and time, not to mention time-dependent studies, which increases such costs even more. Usually, a compromise must be made between computational costs and complexity of both SAS and time-dependent phenomena.

One of the major hurdles for the simulations is the sheer complexity of SAS shape and its internal structures [13]. The patient-specific SAS representation (limited by today's imaging resolution) is comprised of more than ten million voxels. The spatial scale of internal SAS structures is much smaller than the scale of the whole brain. In addition, SAS has many bays that are comparably long and thin regions protruding closer to the parenchyma and there are thin structures that envelope cerebrovascular system (perivascular spaces) [14], therefore, the accurate simulation of the fluid flow inside the SAS requires a substantial amount of computing resources and time.

Until now, the computational complexity was reduced by coarsening and smoothing out the structures of SAS, and as a result, losing spatial information of any thin structures such as bays or major perivascular spaces [7]. Under some high-pressure conditions, such as blood rush into SAS following arterial aneurysm rupture (aneurysmal subarachnoid hemorrhage (aSAH)), bays and perivascular spaces could play a crucial role for the patient's outcome and, therefore, must be included in the CSF flow model. The importance of inclusion of perivascular spaces and bays in the CSF flow model for aSAH patients is clear, as CT scan data of aSAH patients shows that major portion of blood ends up in the perivascular spaces [15]. The importance of patient specific SAS cross-sectional areas could be manifesting in aSAH patients. It was demonstrated that younger aSAH patients tend to develop vasospasms more often than the older aSAH patients [16]. Apart from other mechanisms such as higher vessel elasticity this could also be attributed to the smaller cross-sectional areas of SAS, as with age the cross-sectional area of SAS increases [14].

Therefore, the main goal was to develop a numerical CSF flow model that incorporates patient-specific 3D model encompassing cerebral ventricular system (CVS), cranial SAS (cSAS), and periarterial spaces, which are directly reconstructed from the magnetic resonance imaging (MRI) data with only minimal manual changes required to cut the non-anatomical connections, while all the details were kept up to the MRI resolution, to obtain the maximum morpho/topo correspondence (patient-specificity). A T_2-weighted MRI scans were performed to enhance the visibility of periarterial spaces [14].

In this paper, we present a pilot finite element method (FEM) based model of CSF flow in the detailed, patient-specific cranial subarachnoid space, periarterial space and ventricular system, furthermore, we analyze how to optimize very demanding solution process, by inspecting differences in obtained numerical solutions with different finite element orders, namely P_1 and P_2 (additional information on element orders are provided in methods section *mesh element order*), and in addition we present the initial results obtained with our pilot model, that we hope would spark further discussions and development in this scientific multidisciplinary field.

II. Methods

Approval of all ethical and experimental procedures and protocols was granted by Vilnius Regional Biomedical Research Ethics Committees (Protocol No. 2021/9-1370-847) and performed in line with the Declaration of Helsinki.

A. Subject selection

A single, healthy, 42 years old male subject from Vilnius University Hospital Santaros Clinics was enrolled for this study. The subject had no previous history of neurological or cardiovascular disorders.

B. MRI scan protocol

The brain of the subject was scanned with Philips Achieva 3T MR scanner. During the scanning, the subject was lying supine with his neck in a neutral position. To maximize the contrast of the intracranial CSF, the MRI was obtained by performing the sequence of T_2-weighted Drive HR with the following parameters: TE 226ms, TR 1.6ms, FA 90, section thickness 1.3 mm, voxel size 0.59x0.50x1.3 mm.

C. Segmentation

The 3D Slicer v5.1 software [17], [18], [19] was used for the cranial cerebrospinal fluid space (cCSFS) volume segmentation, its visual inspection and correction, while the COMSOL Multiphysics® v6.0 [20], was used for CSF flow pattern prediction and its visual inspection to identify intricate non-anatomical cCSFS connections. The cCSFS is a space composed of cranial subarachnoid space, periarterial space and ventricular system.

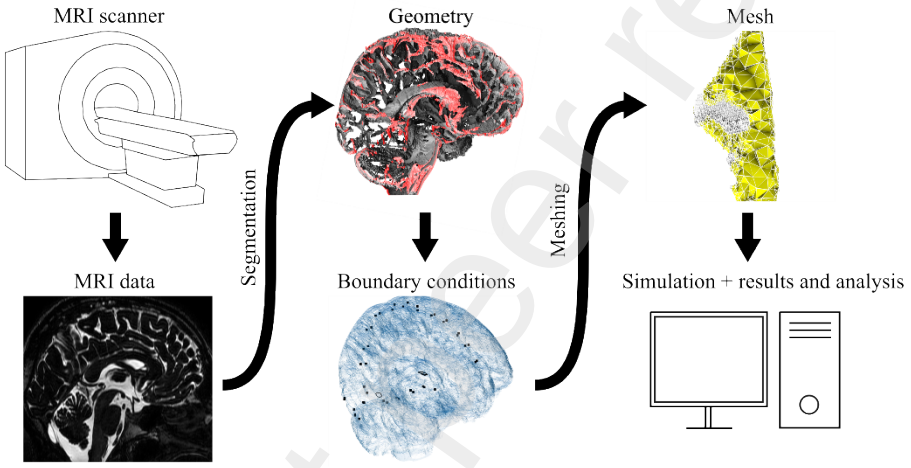

Fig. 1. The workflow chart. MRI scanner was used to obtain the MRI medical imaging data. Segmenting was performed on the medical imaging data to obtain the geometry of patient-specific cCSFS. Obtained geometry was used in the computational fluid dynamics model of CSF flow incorporating boundary conditions: CSF inflow (black loop curves at choroid plexus) and CSF outflow locations (black points close to sinuses). Mesh was generated (here only the fourth ventricle of the cCSFS is shown as mesh density was too high to see individual mesh elements for larger structures: surface mesh is in grey, while the volumetric mesh is in yellow, mesh edges are in white). Finally, the simulations were performed and the CSF flow field parameters were obtained for the analysis.

The final cCSFS segmentation was obtained in several steps. The initial segmentation of cCSFS was obtained using threshold method (in 3D Slicer), which resulted in a few non-anatomical connections, e.g., the direct connections between ventricles and the upper parts of the brain. The non-anatomical connections, which can be classified into obvious and intricate, were cut-off by using the manual cut-delete type segmentation tools (in 3D Slicer), removing only a minimal portion of cCSFS, just enough to cut the non-anatomical connection. The obvious non-anatomical connections were detected by visually inspecting the cCSFS segmentation (in 3D Slicer), while the intricate non-anatomical connections were detected and removed in the iterative procedure of CFD numerical solution and visual inspection of CSF flow patterns (in COMSOL), applying corrections on the cCSFS segmentation (in 3D Slicer) and repeating this procedure until the final, anatomically correct cCSFS segmentation was obtained.

The MRI scanning part was done by a professional radiologist, while the segmentation part was done by both field professionals, namely, radiologist and CFD modeler.

The full workflow chart is depicted in Fig. 1.

D. Numerical model of CSF flow

The main idea of this CFD model is to simulate the net CSF flow within the cCSFS. There are multiple ways to reach this goal. The most comprehensive and most computationally expensive way would be to solve the full Navier Stokes equations for the prescribed amount of heart pulses and evaluate the net CSF flow. Based on [7], the average of about 11 heart pulses were used to obtain net CSF flow (named as "frozen flow field"). However, our current detailed cCSFS would require a significant computing effort in order to obtain the net CSF "frozen flow field". Based on [21], the nonlinear convective effects should be minimal in the SAS, and the mechanisms such as arterial pulsations effect on the CSF flow dynamics are still inconclusive [3]. Therefore, to obtain the net CSF flow we omitted all nonlinearities and solved the stationary case. However, the presented numerical model could be adapted to solve time-dependent phenomena.

1) Governing equations

Based on the Darcy's law, the mean CSF fluid velocity, $\mathbf{u}$, in the cSAS and CVS is determined as follows:

$$\mathbf{u} = -\frac{\kappa}{\mu}\nabla p \qquad (1)$$

where p is the CSF pressure, ∇p is the CSF pressure gradient, κ is the cSAS and CVS permeability and μ is the CSF dynamic viscosity.

For the incompressible flow, the continuity equation is as follows:

$$\nabla \cdot (\rho \mathbf{u}) = 0 \qquad (2)$$

where ρ is the CSF density, $\nabla \cdot$ is the divergence operator.

2) CSF material parameters

The permeability of the cCSFS was prescribed as uniform in the whole area of CSF flow and was set to $\kappa = 2.36 \cdot 10^{-8}$ m^2 [21], accordingly, while the dynamic viscosity $\mu = 7 \cdot 10^{-4}$ Pa·s and density $\rho = 993.45$ kg/m^3 of CSF was that of water.

3) Boundary conditions

A pressure of 10 [mmHg], corresponding to a normotensive intracranial pressure, was prescribed at the presumed locations of choroid plexuses, which acted as the inlet boundary condition for the generation of CSF flow [22]. For the CSF resorption, the point mass source boundary conditions were prescribed at points depicting the presumable locations of arachnoid granulations in Fig. 1. The point mass sources were prescribed in such a way that 80 % of the whole CSF mass flow of 500 ml/day [23] was directed towards the upper part of the brain, while the remaining 20 % was directed towards the lower part of the brain, while the CSF flow between both brain hemispheres was prescribed to be equal.

4) Mesh

The mesh, representing the cCSFS, was generated with the FEM based COMSOL Multiphysics® software and it consisted of more than 19.5 million tetrahedral elements. The mesh element number density was close to 100 tetrahedral elements per 1 mm^3, and it was almost uniform throughout the whole surface of cCSFS. Due to high mesh density, it was hard to visualize any comparably big anatomical structure; therefore, we only visualize the mesh of a smaller, zoomed in, anatomical structure of the fourth ventricle shown in Fig. 1.

5) Mesh element order

The solution accuracy depends on the mesh element order [24]. Tetrahedral finite elements are noted as P. The integration nodes of first-order P_1 element are located only at the corners resulting in a total of four nodes per element, while second-order P_2 elements have six additional integration nodes located at the middle of the edges. The interpolation in P_1 elements is performed in terms of the linear shape functions, while the interpolation on the P2 element is performed in terms of the quadratic shape functions.

For general convection-diffusion driven problems, P_2 mesh elements are expected to be the optimal choice, in terms of accuracy and computational effort. However, our case differs from the general case, as the surface mesh obtained from the segmentation is extremely dense. In general, when the mesh is dense enough, the lower order elements should provide similar results as the higher order elements. Therefore, it is important to evaluate whether the element density is high enough to provide accurate results, so that the significant computation time can be saved by using first-order P_1 elements.

To evaluate the differences in solutions and in the computational effort required between the P_1 and P_2 order elements two numerical modelling studies were performed, of which, in one of the studies mesh was composed of only first-order P_1 elements and in the second study mesh was composed of only second-order P_2 elements. In the case of first-order P_1 elements, the mesh resulted in the $5.6 \cdot 10^6$ number of degrees of freedom (DOF) solved for, while in the case of second-order P_2 elements the number of DOF was $3.5 \cdot 10^7$.

6) Solver settings

The numerical model of the mean CSF flow was solved with the commercial COMSOL Multiphysics v6.0 software, which uses Finite Element Method (FEM) as a basis for the numerical modelling. The stationary solver included the linear iterative Generalized Minimal RESidual method (GMRES) solver and the Smoothed Aggregation Algebraic MultiGrid (SAAMG) preconditioner. In addition, SAAMG was combined with Successive Over-Relaxation (SOR) line pre- and post- smoothers and a coarse PARallel DIrect SOlver (PARDISO). The relative tolerance of the stationary solver was set to $1 \cdot 10^{-3}$.

E) Methods for geometric and CSF flow analysis

To analyze CSF flow, we follow a similar procedure as developed in [7]. We have calculated projections starting from the full 3D cCSFS model to the 2D *xz* plane and then to the 1D *z* axis (Fig. 2). *z* axis corresponds to the up/down axis, *x* axis corresponds to left/right axis, while the *y* axis corresponds to front/back axis. However, the projection method cannot be applied to evaluate the perimeter; therefore, it was evaluated by slicing the mesh at 1 mm intervals and evaluating the length of the resulting curves.

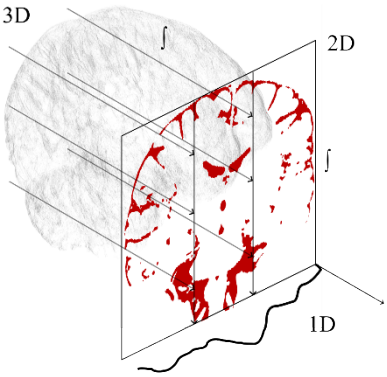

Fig. 2. The scheme of projection operation. The projection of the selected parameter is calculated by integrating lines. Two steps are required to go from 3D->2D->1D representation. In our case, the projections from 3D to 2D were calculated on the front/back *y* axis, while from 2D to 1D it was calculated on the left/right *x* axis. Additionally, the spaces of interest (CVS and SAS) were separated.

For the evaluation of the CSF flow field parameters, the cCSFS was separated into two distinct parts, the cSAS and CVS. cSAS was composed of cranial subarachnoid space and periarterial space (not all periarterial space was reconstructed as the reconstruction was limited by MRI T_2-weighted resolution). CVS has large regions where the flow is almost zero in *z* axis, therefore, it was filtered by applying $>U_{mean}$ filter, where U_{mean} is the average CSF flow velocity in CVS, so that it would only include the space where the flow direction is mostly *z* axis dominant. In addition, CVS has two regions where the upward flow is dominant in one location and downward flow is dominant in other, therefore, the more important location with downward flow direction is used for the flow analysis. The following operations resulted in a filtered cerebral ventricular system (fCVS).

The hydraulic diameter was calculated as $D_H = 4 \cdot S/P$, where S is the cross-sectional area, P is the perimeter of the cross-section. After obtaining the D_H it was easy to evaluate the Reynolds number as $Re = \rho u D_H/\mu$.

III. Results

Firstly, we present the geometric parameters of cSAS and CVS. Secondly, as the numerical simulations of the CSF flow in a patient-specific cSAS and CVS are time demanding tasks, we compare the results obtained with P_1 and P_2 finite elements and show that for this specific problem the computational time required could be reduced with minimal impact on the solution accuracy by using the P1 finite elements. Finally, we present the hydrodynamic parameters of the CSF flow in the cSAS and CVS and analyze the CSF flow results.

A. Geometric parameters

The volume and surface area values presented in Table I are obtained from our 3D model of the cCSFS. We note that the accuracy of these values is limited by the tomography imaging (in this case 3T MRI) resolution.

TABLE I. Cranial cerebrospinal fluid space geometric parameters.

Geometric entity:	Volume (ml)	Surface area (m^2)
Ventricular system	18.3	0.015
Subarachnoid space	180.3	0.307
CSF space (cCSFS)	198.6	0.322

The obtained volume values due fall into the expected range of 150-400 ml [7]. However, currently, there is no experimental data regarding the surface area of the cCSFS, which could be an important parameter for the interstitial transport of various substances [25].

B. Net CSF flow modelling

Two stationary numerical simulations of the net CSF flow in the reconstructed patient-specific cCSFS were performed using P_1 (4 node linear elements) and P_2 (10 node quadratic elements), respectively. The net CSF flow was modelled based on Darcy's law and continuity equations. All simulations were performed on a single Kaunas University of Technology (KTU) cluster node with 2xAMD EPYC 7452 32-core processors and 512 GB of RAM. In both cases, the solution converged in 1 iteration, and for the P_1 elements it took almost 5 min., while with the P_2 elements it took almost 20 min., consuming about 30 GB of random access memory (RAM) in P_1 case and about 150 GB RAM in P_2 case. Simulations provided spatial distribution (field) of pressure and its derivative values (velocity, etc.).

C. Comparison of the net CSF flow field results obtained by solving the model with P_1 and P_2 elements.

Several different approaches were used to compare the net CSF flow field values obtained by solving the model with P_1 and P_2 elements.

Firstly, three longest streamlines originating in the choroid plexus and following the CSF flow paths in left, right and middle brain regions were calculated from the CSF flow solution, which was obtained with P_2 elements. The overall similarity between CSF flow velocity field magnitude values of P_1 and P_2 solutions resulting on these streamlines was evaluated by calculating the correlation coefficient, mean value proportion and similarity coefficient based on [26]. The correlation coefficient for the CSF flow velocity field magnitude values [left, right, middle] paths was [0.9932, 0.9964, 0.9967], the mean value proportion was [0.9862, 0.9879, 0.9925] and the similarity coefficient was [0.9635, 0.9728, 0.9701]. All these values indicate strong similarity between solutions obtained with P_1 and P_2 order elements.

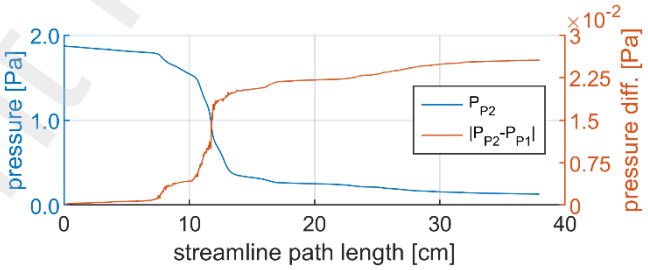

Fig. 3. Pressure obtained on the streamline starting at the choroid plexus of the right ventricle and following a path throughout the right-brain hemisphere up to the arachnoid granulations. P_2 solution in blue, difference in pressure between P_2 and P_1 solutions in orange.

The small transmantle pressure (the instantaneous pressure difference between the lateral ventricles and the cranial subarachnoid space) value of 1.8 Pa was obtained that was sufficient to drive the prescribed net CSF flow rate of 500 ml/day (Fig. 3).

The difference between pressures obtained with P_1 and P_2 elements accumulated throughout the CSF flow path and its increase was proportional to the velocity (Fig. 3). The difference of obtained transmantle pressures was only 1.4% between P_1 and P_2 solutions.

Finally, the volumetric differences between the CSF flow field values of the corresponding locations of P_1 and P_2 solutions were evaluated. To account for the varying mesh element size, the CSF flow velocity was multiplied by the mesh element mass and in this way the momentum, M (kg·m/s), of the mesh element was obtained. Further on, the difference of M between P_1 and P_2 solutions were calculated. It was obtained that about 70% of the elements had the difference in momentum lower than 5 %, while about 20 % had it ranging from 5% to 10% while the rest of the elements had it higher than 10% (Fig. 4).

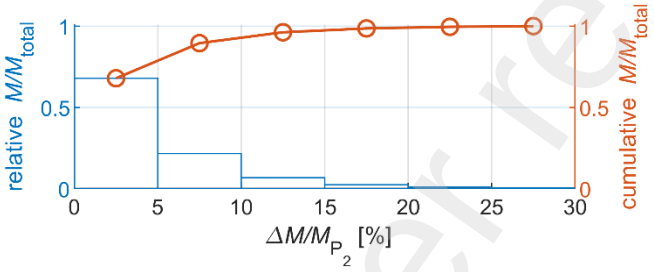

Fig. 4. The relative and cumulative ratio of element momentum, M (kg·m/s) with the total system's element momentum, which falls in the specific range of relative difference between P_1 and P_2 solutions.

All these different P_1, P_2 solution evaluation approaches showed, that the differences between the solution obtained with P_1 and P_2 elements are not significant, therefore, for these types of studies P_1 elements can be used to reduce the computational effort and time.

D. CSF flow analysis

The CSF velocity magnitude projected on the XZ plane, U_{xz}, was used to visualize the modelled CSF flow patterns, which distribution in fCVS is shown in Fig. 5 a), while for cSAS it is shown in Fig. 5 b). From these patterns it can be deduced that the CSF flow velocity distribution for the fCVS was fairly symmetric around the flow path center (the flow path center is almost parallel to the x=0 axis). In the fCVS, the U_{xz} was highest at the aqueduct of Sylvius and reached about 0.4 cm/s, while in the cSAS it was highest at locations, which forms the CSF up flow from the CVS to the arachnoid granulations. Also, for the cSAS, some local differences of the velocities can be seen between the left and the right brain hemispheres, as the velocities were locally higher in the leftmost part of the brain Fig. 5 b). This can be attributed to local cSAS anatomical differences between brain hemispheres.

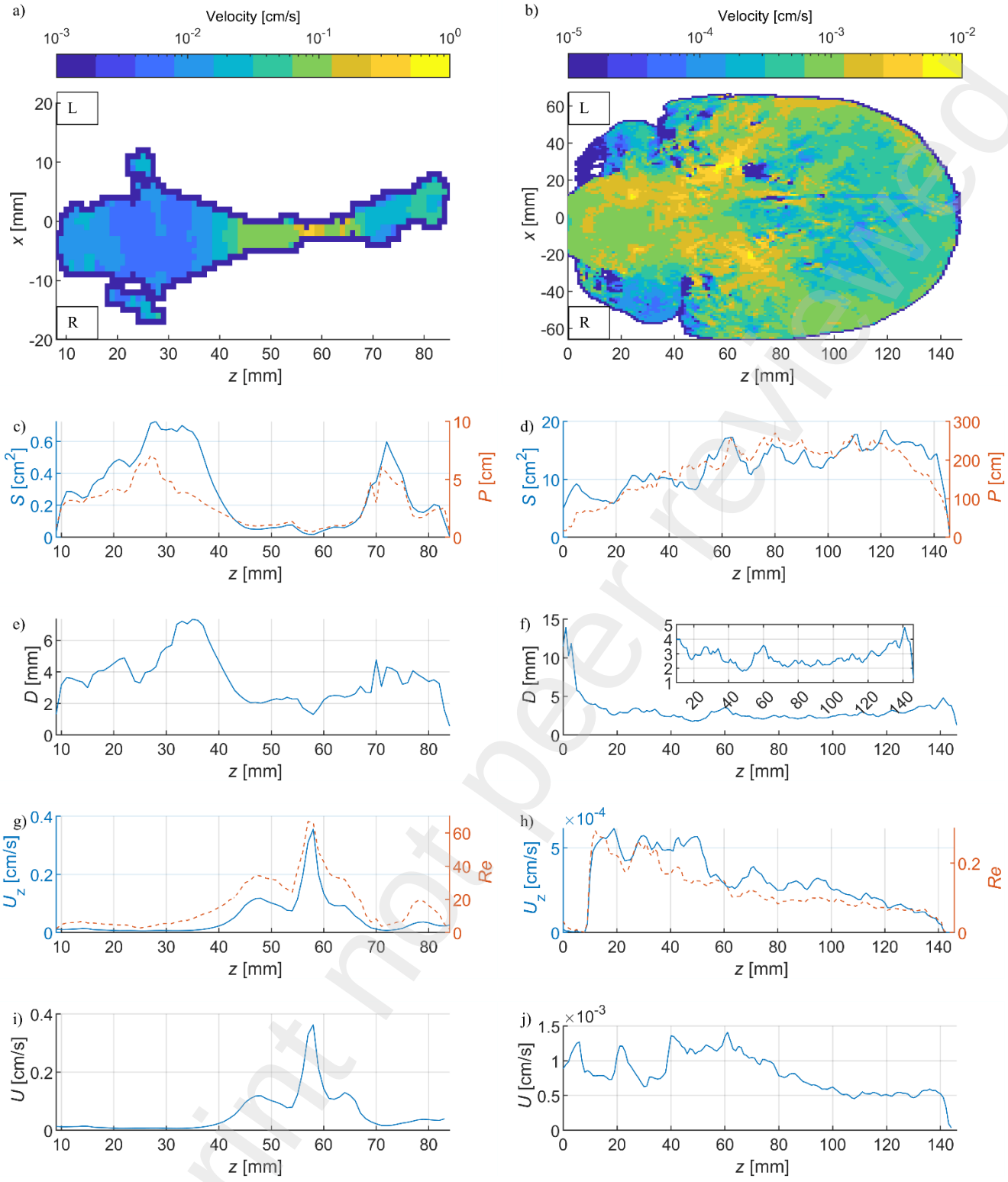

Fig. 5. Projections on *xz* plane of CSF flow velocity magnitude, *U*, and projections on *z* axis of cross-sectional area, *S*, perimeter, *P*, hydraulic diameter, *D*, velocity magnitude, *U* and velocity *z* component, U_z and Reynolds number, *Re*, for fCVS a), c), e), g), i) and cSAS b), d), f), h), j), respectively.

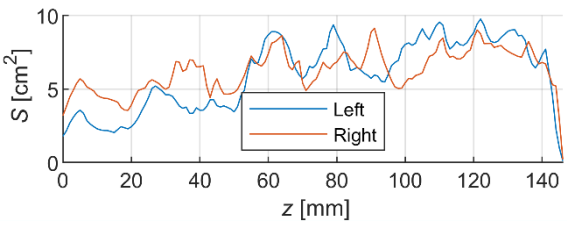

Fig. 6. The cross-sectional area, S, of left and right brain hemispheres.

The average velocity magnitude in the fCVS was $2 \cdot 10^{-2}$ cm/s, while in the cSAS it was $8 \cdot 10^{-4}$ cm/s, and the average velocity magnitude on the left-brain hemisphere was higher than on the right-brain hemisphere as it was $8.3 \cdot 10^{-4}$ cm/s, while on the right-brain hemisphere it was $7.7 \cdot 10^{-4}$ cm/s. As the CSF flow rates were prescribed to be equal between brain hemispheres, the difference in average velocities is due to the difference in cSAS cross-sectional areas between brain hemispheres (Fig. 6). The average cross-sectional area in main flow direction (z axis) in cSAS on the left-brain hemisphere was 5.85 cm^2, while on the right-brain hemisphere it was 6.11 cm^2.

The cross-sectional area of fCVS in z axis was fluctuating and reached the highest value of almost 0.73 cm^2 at the fourth ventricle and the lowest value of almost $1.6 \cdot 10^{-2}$ cm^2 at the aqueduct of Sylvius (Fig. 5 c)), while cross-sectional area of the cSAS on z axis in the cerebrum part of the brain fluctuated around the average value of 15 cm^2 and in the cerebellum part of brain it fluctuated around the average value of around 8 cm^2 (Fig. 5 d)). The average cross-sectional area of fCVS was 0.29 cm^2, while of the cSAS it was 12.28 cm^2, resulting in a cross-sectional area ratio cSAS/fCVS of 42.35.

The projected perimeter distributions on z axis in principle followed the cross-sectional area distribution (Fig. 5 c)) and Fig. 5 d)), indicating of a similar hydraulic diameter throughout the z axis. This is shown in Fig. 5 e) and Fig. 5 f), where the hydraulic diameter for the fCVS was in a range from about 1 to 10 mm with the average value of 5 mm with a comparably low dispersion. The hydraulic diameter in most of the SAS was in a range of about 2 to 4 mm with the average of 3 mm and also with low dispersion.

The velocity in z axis in the fCVS was from $5 \cdot 10^{-3}$ cm/s to almost 0.4 cm/s and the Reynolds number of the CSF flow was in the range from 1 to almost 70 (Fig. 5 g)). The highest velocity and Reynold number was at the aqueduct of Sylvius, while the lowest velocity and Reynolds number was at the fourth ventricle. The z component of velocity in the cSAS, where it was relevant, was from around $1 \cdot 10^{-4}$ cm/s to $6 \cdot 10^{-4}$ cm/s and the Reynolds number of CSF flow was in the range from 0.05 to 0.3 (Fig. 5 h)). The highest z component of velocity was at the cerebellum part of the brain. Overall, the dominance of the z component of the velocity was decreasing going towards the arachnoid granulations.

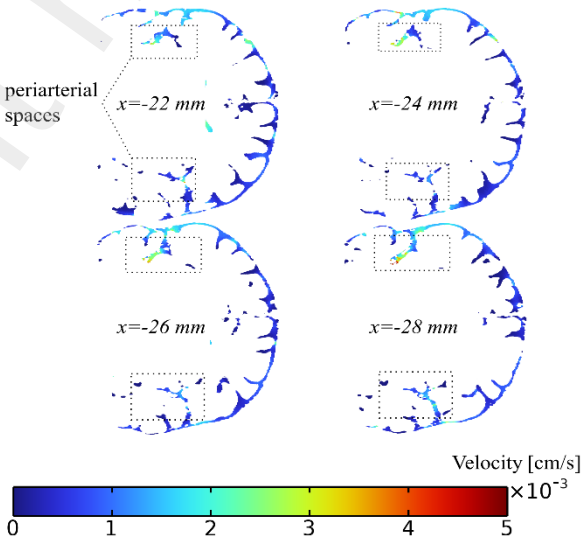

Fig. 7. CSF flow magnitude on zy plane at several x locations, where periarterial spaces are present a) at x=-22 mm, b) at x=-24 mm, c) at x=-26 mm, d) at x=-28 mm.

The velocity magnitude in the fCVS was similar to velocity's z component and was in range from $5 \cdot 10^{-3}$ cm/s to almost 0.4 cm/s (Fig. 5 i)). The highest velocity was at the aqueduct of Sylvius, while the lowest velocity was at the fourth ventricle. The velocity magnitude in the cSAS, where it was relevant, was from around $0.5 \cdot 10^{-3}$ cm/s to almost $1.5 \cdot 10^{-3}$ cm/s (Fig. 5 j)). The highest velocity magnitude was at the cerebellum part of the brain. The CSF flow velocity in periarterial spaces was nonuniform and when comparing left and right brain sides it was also non symmetric (Fig. 7). The average velocity magnitude in periarterial spaces was around $1.5 \cdot 10^{-3}$ cm/s, while in the subarachnoid space it was $7.7 \cdot 10^{-4}$ cm/s that is almost two times higher.

IV. Discussion

In previous works it was shown that CSF flow dynamics could have influence on the patient outcomes after subarachnoid hemorrhage [27], cerebral ischemia [28], multiple sclerosis [29], or traumatic brain injury [30]. On the basis of the timely evaluation of the patient-specific CSF flow patterns clinicians could take appropriate decisions and measures, and improve various clinical evolutions and patient outcomes.

The inclusion of periarterial spaces is important, especially when considering the clearance of unwanted substances such as leaked blood from the aneurysmal rupture [27]. In addition, periarterial spaces allow evaluation of the direct contact between CSF, leaked blood and artery walls.

In this paper we presented a method/model that included cCSFS geometry comprised of CVS, SAS and to the maximum allowed extent by today's current imaging techniques, the periarterial spaces, which was reconstructed from the high-resolution MRI scan data with a minimal manual intervention required to cut the non-anatomical connections. The resulting perivascular spaces were highly connected to the SAS and due to this, the CSF flow rate was similar between periarterial spaces and the cSAS, but the average velocity in periarterial space was about 2 times higher, which is due to the lower cross-sectional areas of periarterial spaces.

The minimal manual interventions were mostly in the areas between ventricles and the parts of the cSAS, however, whether these connections are truly non-anatomical remains to be discovered, as some studies on rats indicate that there could be direct connections between ventricles and the cSAS [31].

The obtained surface mesh follows the segmentation of the high resolution T_2-weighted MRI. In most parts this creates an overly dense mesh, which would lead to the inefficient use of computational power. One way to reduce the density of this mesh is to use surface smoothing procedures. However, any meaningful attempts to smoothen out the resulting surface and in this way reduce the geometrical complexity by allowing larger triangles to be used and simultaneously retain bays and perivascular spaces, always leads to the problems of self-intersections and requires removal of many inside protrusions, making smoothing not applicable. Another option is to reduce the discretization order (P_2 to P_1 as an example) as we did in this paper. The CSF flow results obtained between P_1 and P_2 elements resulted in a difference, which are comparably low, and it is known that given enough mesh density both solutions should provide similar results [32]. In this paper we have showed that when using the minimally manually adjusted segmentations directly obtained from the high-resolution MRI, and when using finite element formulations to solve for Darcy flow equations one can use the P_1 elements and expect a solution that in most parts should be within 10% of relative error from the P_2 solution. In this way, effects on the increase in the computations required due to overly dense mesh, of which due to its specificity cannot be reduced

by the smoothing procedures, is reduced by the possibility to use the P_1 elements. The uncertainties in CSF flow boundary conditions are at least an order of magnitude higher than the difference between P_1 and P_2 elements.

Although there are at least several studies involving the CSF flow dynamics in subarachnoid space [10], [11], [8], only the [7] provided an extensive analysis on geometric and hydrodynamic parameters that we can directly compare with. The average hydraulic diameter in SAS obtained in our study was about 3 mm, while in [7] it was 6.2 mm. This twofold difference is mainly a result of geometric interventions applied in their study to coarsen and smooth out the SAS in order to obtain a continuous (without gaps) SAS structure. Anatomically, SAS should be continuous as opposed to our non-continuous SAS, however, the regions, which lacks continuation means that the cross-sectional area of the SAS in these areas were lower than the MRI resolution and so the inclusions of these areas would reduce the hydraulic diameter even more. In our study we aimed to directly use the data provided by the MRI with minimal interventions, therefore, no additional connections were made in SAS to make it fully continuous.

Our obtained transmantle pressure value of 1.8 Pa is on par with the experimental and numerical modelling results performed by others. Based on experimental evidence in [33] it was postulated that the transmantle pressure was less than ~30 Pa, while based on the numerical modelling results of [34] transmantle pressure was about 0.2+-0.4 Pa.

Our obtained mean CSF velocity in periarterial space was $1.5 \cdot 10^{-3}$ cm/s. There are no experimental studies on humans that measures the CSF flow velocity in perivascular spaces, and based on the animal measurements the average CSF velocity in mice was about $2 \cdot 10^{-3}$ cm/s [35]. The theoretical considerations made by [36] suggests that in human perivascular spaces this velocity should be around ten times higher. To understand the underlying discrepancies the mechanism of CSF flow driving forces must be considered. Experimental studies on animals showed that the CSF flow throughout the perivascular spaces is driven by the arterial wall motion [35], later experiments have added more reliability to this claim [37]. It was also shown that the respiratory cycle is not the main cause for the unidirectional CSF flow throughout the perivascular space [35]. In [38] have shown that tracer injected into the human lumbar CSF, have spread throughout the whole brain's subarachnoid space and the extravascular compartments, such as perivascular spaces. The spreading was faster than if only the diffusion would be responsible for it, showing that there is some additional mechanism driving the CSF flow. The fact that the tracer had higher concentrations in the regions close to vessels shows that the arterial pulsations must play a role in CSF bulk movement and as a result be closely related with that additional mechanism. There are at least two hypotheses on how this mechanism involving the arterial wall motion is acting: the peristalsis (both slow and high frequencies) and the shear augmented dispersion. It seems that high frequency (cardiopulmonary) peristalsis under right conditions [1] and the shear augmented dispersion [39] are good candidates for CSF driving forces. In addition, recent studies on mice [40] and humans [41] have shown that during sleep a slow oscillation (low frequency peristalsis) in vessel diameter (slow vasomotion) occurs and it increases velocity in the PVS up to levels similar to the bulk CSF flow and dispersion up to levels comparable to cardiac-driven oscillations. Based on the [25] the circadian (sleep-wake) cycle could be an important regulator of the resistance to flow in periarterial and downstream CSF flow locations. We can consider one important case: if the CSF velocity in human periarterial space should be much higher than we have obtained, this means that the resistivity to flow in the periarterial space and downstream should be reduced, resulting in higher CSF that comes from ventricles flow sink towards periarterial spaces.

The rate of CSF flow in subarachnoid space could still be the same only if the CSF that came into periarterial space and all the downstream locations would in the end up flowing again in cSAS.

Our obtained mean CSF velocity in cSAS of $8 \cdot 10^{-4}$ cm/s is almost twofold greater than that obtained by [7] of $4.5 \cdot 10^{-4}$ cm/s. This can be directly related to more than twofold lower hydraulic diameter of our cCSFS model.

A. Limitations and future work

Currently, due to technical limitations, the full in vivo CSF flow representation cannot be obtained, not even mentioning to do this in a timely manner [7]. Phase Contrast Magnetic Resonance Imaging MRI (PCMRI) is the state-of-the-art technique allowing estimation of CSF flow patterns; however, it is usually used to evaluate specific only 2D planes of interest (not full 3D), also it is a very time-consuming procedure, and the current resolution of PCMRI could be too low to measure CSF flow with enough accuracy [42]. Due to this the picture of full CSF flow pathway is not complete. The actual cCSFS should at least be composed of ventricles, subarachnoid space and perivascular spaces [22]. And although in our study we performed T_2-weighted MRI, which is the best available technique for this purpose, it cannot capture all the perivascular spaces, therefore, current cSAS 3D anatomical model is limited by today's imaging techniques.

In addition, up till now, there is no clinical data whether our made assumption of CSF flow rate distribution in upper brain region corresponding to 80 % and lower brain regions corresponding to 20 % of overall CSF flow rate and symmetric CSF flow rate between brain hemispheres is correct and therefore, more experimental data is needed to improve the knowledge on the CSF flow pathways.

In mice, periarterial space is an open nonporous space filled with fluid when surrounding large arteries [43]. This has been verified by experimentally observing a parabolic velocity profile across surface para-arterial spaces in vivo and a collapsed PVS postmortem (indicating no supporting tissue) [43]. It is postulated that the PVS becomes porous downstream along arterioles and capillaries. Similarly, the same can also be expected for humans. Our model does not encompass full glymphatic system, which is an interdependent system, therefore, currently, there is no added benefit to making well resolved model of part of the system, and therefore, to simplify things we assumed uniform permeability and a Darcy flow equation throughout the whole cCSFS.

CSF flow in open periarterial spaces should be solved using the Navier-Stokes equations, and in such a way the resistivity to flow in periarterial spaces due to their anatomical structure should be reduced several times [6]. However, several boundary layers in the computational mesh are required to resolve the flow gradients, which due to geometrical model complexity and mesh generation intricacies is hard, but not impossible. Therefore, future studies could be aimed in adding boundary layers.

Only one patient-specific case was analyzed. With more cases we may find out how well the obtained results generalize, however more emphasis should be made on the improvements on CSF flow pathways and resistance to CSF flow evaluation.

VI. Conclusion

A numerical CSF flow FEM based model was presented that incorporated patient-specific 3D model encompassing cerebral ventricular system (CVS), cranial SAS (cSAS), and periarterial spaces reconstructed from T_2-weighted MRI. It was shown that

computational effort required for such a complex system can be sufficiently reduced with a minor impact on accuracy by using first-order P_1 elements instead of the second-order P_2 elements.

Our model showed that a constant net CSF flow of 500 ml/day was maintained, while the transmantle pressure was 1.8 Pa. Also, our obtained mean CSF velocity in periarterial space was $1.5 \cdot 10^{-3}$ cm/s, while mean CSF velocity in cSAS was $8 \cdot 10^{-4}$ cm/s. Further on, the solution accuracy obtained enables timely predictions of CSF flow patterns that could find its use in clinical practice for patients of subarachnoid hemorrhage, cerebral ischemia, multiple sclerosis, traumatic brain injury or hydrocephalus.

VI. Conflict of Interest

V. Petkus, A. Dziugys, A. Preiksaitis, E. Misiulis, G. Skarbalius, R. Navakas, T. Iesmantas, M. Serpytis, S. Lukosevicius, V. Ratkunas, A. Barkauskiene, I. Lapinskiene, S. Rocka, R. Alzbutas have patent pending for invention related to method for early warning of cerebral vasospasm after subrachnoid hemorrhage based on numerical modelling of cerebrospinal fluid flow.

VII. Acknowledgment

This work was supported by the European Regional Development Fund with the Research Council of Lithuania under grant agreement (No.01.2.2-LMT-K-718-03-0091). The authors acknowledge the High Performance Computing Center (HPCC) at Kaunas University of Technology for providing computational resources that have contributed to the research results reported within this paper. URL: https://aicentre.ktu.edu/high-performance-computing-hpc-solutions/.

VII. Ethics

This work involved human subjects in its research. Approval of all ethical and experimental procedures and protocols was granted by Vilnius Regional Biomedical Research Ethics Committees (Protocol No. 2021/9-1370-847) and performed in line with the Declaration of Helsinki.

References

[1] A. Ladrón-de-Guevara, J. K. Shang, M. Nedergaard, and D. H. Kelley, “Perivascular pumping in the mouse brain: Improved boundary conditions reconcile theory, simulation, and experiment,” *J Theor Biol*, vol. 542, p. 111103, Jun. 2022, doi: 10.1016/j.jtbi.2022.111103.

[2] C. Daversin-Catty, V. Vinje, K. A. Mardal, and M. E. Rognes, “The mechanisms behind perivascular fluid flow,” *PLoS One*, vol. 15, no. 12 December, Dec. 2020, doi: 10.1371/journal.pone.0244442.

[3] R. T. Kedarasetti, P. J. Drew, and F. Costanzo, “Arterial pulsations drive oscillatory flow of CSF but not directional pumping,” Sci Rep, vol. 10, no. 1, p. 10102, Jun. 2020, doi: 10.1038/s41598-020-66887-w.

[4] M. Asgari, D. de Zélicourt, and V. Kurtcuoglu, “Glymphatic solute transport does not require bulk flow,” Sci Rep, vol. 6, no. 1, p. 38635, Dec. 2016, doi: 10.1038/srep38635.

[5] N. Yokoyama, N. Takeishi, and S. Wada, “Cerebrospinal fluid flow driven by arterial pulsations in axisymmetric perivascular spaces: Analogy with Taylor’s swimming sheet,” *J Theor Biol*, vol. 523, p. 110709, Aug. 2021, doi: 10.1016/j.jtbi.2021.110709.

[6] V. Vinje, E. N. T. P. Bakker, and M. E. Rognes, “Brain solute transport is more rapid in periarterial than perivenous spaces,” Sci Rep, vol. 11, no. 1, p. 16085, Aug. 2021, doi: 10.1038/s41598-021-95306-x.

[7] M. Khani et al., “In vitro and numerical simulation of blood removal from cerebrospinal fluid: Comparison of lumbar drain to Neurapheresis therapy,” Fluids Barriers CNS, vol. 17, no. 1, Mar. 2020, doi: 10.1186/s12987-020-00185-5.

[8] K. Tangen, N. S. Narasimhan, K. Sierzega, T. Preden, A. Alaraj, and A. A. Linninger, “Clearance of Subarachnoid Hemorrhage from the Cerebrospinal Fluid in Computational and In Vitro Models,” Ann Biomed Eng, vol. 44, no. 12, pp. 3478–3494, Dec. 2016, doi: 10.1007/s10439-016-1681-8.

[9] M. Khani et al., “Impact of Neurapheresis System on Intrathecal Cerebrospinal Fluid Dynamics: A Computational Fluid Dynamics Study,” J Biomech Eng, vol. 142, no. 2, Feb. 2020, doi: 10.1115/1.4044308.

[10] S. Vandenbulcke, T. De Pauw, F. Dewaele, J. Degroote, and P. Segers, “Computational fluid dynamics model to predict the dynamical behavior of the cerebrospinal fluid through implementation of physiological boundary conditions,” Front Bioeng Biotechnol, vol. 10, Nov. 2022, doi: 10.3389/fbioe.2022.1040517.

[11] M. Khani et al., “Human in silico trials for parametric computational fluid dynamics investigation of cerebrospinal fluid drug delivery: impact of injection location, injection protocol, and physiology,” Fluids Barriers CNS, vol. 19, no. 1, p. 8, Jan. 2022, doi: 10.1186/s12987-022-00304-4.

[12] S. J. Sincomb et al., “Transmantle Pressure Computed from MR Imaging Measurements of Aqueduct Flow and Dimensions,” American Journal of Neuroradiology, vol. 42, no. 10, pp. 1815–1821, Aug. 2021, doi: 10.3174/ajnr.A7246.

[13] P. Saboori and A. Sadegh, “Histology and Morphology of the Brain Subarachnoid Trabeculae,” Anat Res Int, vol. 2015, pp. 1–9, May 2015, doi: 10.1155/2015/279814.

[14] J. M. Wardlaw et al., “Perivascular spaces in the brain: anatomy, physiology and pathology,” Nat Rev Neurol, vol. 16, no. 3, pp. 137–153, Mar. 2020, doi: 10.1038/s41582-020-0312-z.

[15] R. L. Macdonald and T. A. Schweizer, “Spontaneous subarachnoid haemorrhage,” The Lancet, vol. 389, no. 10069, pp. 655–666, Feb. 2017, doi: 10.1016/S0140-6736(16)30668-7.

[16] M. S. Walid, G. Sahiner, D. R. Robinson, and J. S. Robinson, “The Relationship between Pulmonary Dysfunction and Age in Vasospasm Patients Receiving Triple H Therapy.,” J Vasc Interv Neurol, vol. 4, no. 2, pp. 29–33, Jul. 2011, [Online]. Available: http://www.ncbi.nlm.nih.gov/pubmed/22518269

[17] https://www.slicer.org/

[18] R. Kikinis, S. D. Pieper, and K. G. Vosburgh, “3D Slicer: A Platform for Subject-Specific Image Analysis, Visualization, and Clinical Support,” in Intraoperative Imaging and Image-Guided Therapy, New York, NY: Springer New York, 2014, pp. 277–289. doi: 10.1007/978-1-4614-7657-3_19.

[19] A. Fedorov et al., “3D Slicer as an image computing platform for the Quantitative Imaging Network,” Magn Reson Imaging, vol. 30, no. 9, pp. 1323–1341, Nov. 2012, doi: 10.1016/j.mri.2012.05.001.

[20] COMSOL Multiphysics® v. 6.1. www.comsol.com. COMSOL AB, Stockholm, Sweden.

[21] S. Gupta, M. Soellinger, P. Boesiger, D. Poulikakos, and V. Kurtcuoglu, “Three-Dimensional Computational Modeling of Subject-Specific Cerebrospinal Fluid Flow in the Subarachnoid Space,” J Biomech Eng, vol. 131, no. 2, Feb. 2009, doi: 10.1115/1.3005171.

[22] J. Wan, S. Zhou, H. J. Mea, Y. Guo, H. Ku, and B. M. Urbina, “Emerging Roles of Microfluidics in Brain Research: From Cerebral Fluids Manipulation to Brain-on-a-Chip and Neuroelectronic Devices Engineering,” Chem Rev, vol. 122, no. 7, pp. 7142–7181, Apr. 2022, doi: 10.1021/acs.chemrev.1c00480.

[23] G. A. Rosenberg, “Cerebrospinal Fluid: Formation, Absorption, Markers, and Relationship to Blood-Brain Barrier. Formation, Absorption, Markers, and Relationship to Blood-Brain Barrier” in Primer on Cerebrovascular Diseases: Second Edition, Elsevier Inc., 2017, pp. 25–31. doi: 10.1016/B978-0-12-803058-5.00004-7.

[24] D. Eller, “Fast, Unstructured-Mesh Finite-Element Method for Nonlinear Subsonic Flow,” J Aircr, vol. 49, no. 5, pp. 1471–1479, Sep. 2012, doi: 10.2514/1.C031738.

[25] D. H. Kelley and J. H. Thomas, “Cerebrospinal Fluid Flow,” Annu Rev Fluid Mech, vol. 55, no. 1, pp. 237–264, Jan. 2023, doi: 10.1146/annurev-fluid-120720-011638.

[26] A. Džiugys, R. Navakas, and N. Striūgas, “A Normalized Parameter for Similarity/Dissimilarity Characterization of Sequences,” Informatica, vol. 26, no. 2, pp. 241–258, Jan. 2015, doi: 10.15388/Informatica.2015.47.

[27] J. Zhou, P. Guo, Z. Guo, X. Sun, Y. Chen, and H. Feng, “Fluid metabolic pathways after subarachnoid hemorrhage,” J Neurochem, vol. 160, no. 1, pp. 13–33, Jan. 2022, doi: 10.1111/jnc.15458.

[28] H. Mestre et al., “Cerebrospinal fluid influx drives acute ischemic tissue swelling,” Science (1979), vol. 367, no. 6483, pp. 1198–1199, Mar. 2020, doi: 10.1126/science.aax7171.

[29] K. Rammohan, “Cerebrospinal fluid in multiple sclerosis,” Ann Indian Acad Neurol, vol. 12, no. 4, p. 246, 2009, doi: 10.4103/0972-2327.58282.

[30] H. Zetterberg, D. H. Smith, and K. Blennow, “Biomarkers of mild traumatic brain injury in cerebrospinal fluid and blood,” Nat Rev Neurol, vol. 9, no. 4, pp. 201–210, Apr. 2013, doi: 10.1038/nrneurol.2013.9.

[31] K. N. Magdoom, A. Brown, J. Rey, T. H. Mareci, M. A. King, and M. Sarntinoranont, “MRI of Whole Rat Brain Perivascular Network Reveals Role for Ventricles in Brain Waste Clearance,” Sci Rep, vol. 9, no. 1, p. 11480, Aug. 2019, doi: 10.1038/s41598-019-44938-1.

[32] M. A. McCarthy, C. T. McCarthy, V. P. Lawlor, and W. F. Stanley, “Three-dimensional finite element analysis of single-bolt, single-lap composite bolted joints: part I—model development and validation,” Compos Struct, vol. 71, no. 2, pp. 140–158, Nov. 2005, doi: 10.1016/j.compstruct.2004.09.024.

[33] B. Cohen, A. Voorhees, and T. Wei, “Magnetic resonance velocity imaging derived pressure differential using control volume analysis,” Fluids Barriers CNS, vol. 8, no. 1, p. 16, Dec. 2011, doi: 10.1186/2045-8118-8-16.

[34] P. Holmlund, “Fluid dynamic principles for analysis of intracranial pressure control : application towards space medicine and hydrocephalus,” 2019.

[35] H. Mestre et al., “Flow of cerebrospinal fluid is driven by arterial pulsations and is reduced in hypertension,” Nat Commun, vol. 9, no. 1, p. 4878, Nov. 2018, doi: 10.1038/s41467-018-07318-3.

[36] F. W. Schermer and D. K. Jain, “Computational modelling of cerebrospinal fluid flow in perivascular spaces,” University of Twente, Twente, 2022.

[37] A. Raghunandan et al., “Bulk flow of cerebrospinal fluid observed in periarterial spaces is not an artifact of injection,” Elife, vol. 10, Mar. 2021, doi: 10.7554/eLife.65958.

[38] G. Ringstad et al., “Brain-wide glymphatic enhancement and clearance in humans assessed with MRI,” JCI Insight, vol. 3, no. 13, Jul. 2018, doi: 10.1172/jci.insight.121537.

[39] M. Keith Sharp, R. O. Carare, and B. A. Martin, “Dispersion in porous media in oscillatory flow between flat plates: applications to intrathecal, periarterial and paraarterial solute transport in the central nervous system,” Fluids Barriers CNS, vol. 16, no. 1, p. 13, Dec. 2019, doi: 10.1186/s12987-019-0132-y.

[40] L. Bojarskaite et al., “Sleep cycle-dependent vascular dynamics in male mice and the predicted effects on perivascular cerebrospinal fluid flow and solute transport,” Nat Commun, vol. 14, no. 1, p. 953, Feb. 2023, doi: 10.1038/s41467-023-36643-5.

[41] P. K. Eide, V. Vinje, A. H. Pripp, K.-A. Mardal, and G. Ringstad, “Sleep deprivation impairs molecular clearance from the human brain,” Brain, vol. 144, no. 3, pp. 863–874, Apr. 2021, doi: 10.1093/brain/awaa443.

[42] O. Balédent, Z. Czosnyka, and M. Czosnyka, “‘Bucket’ cerebrospinal fluid bulk flow—is it a fact or a fiction?,” Acta Neurochir (Wien), vol. 161, no. 2, pp. 257–258, Feb. 2019, doi: 10.1007/s00701-018-3731-5.

[43] F. Min Rivas et al., “Surface periarterial spaces of the mouse brain are open, not porous,” J R Soc Interface, vol. 17, no. 172, p. 20200593, Nov. 2020, doi: 10.1098/rsif.2020.0593.